Maddox, S.J. and Valiante, E. and Cigan, P.J. and Dunne, L. and Eales, S. and Smith, M.W.L. and Dye, S. and Furlanetto, C. and Ibar, E. and Zotti, G. de and Millard, J.S. and Bourne, N. and Gomez, H.L. and Ivison, R.J. and Scott, D. and Valtchanov, I. (2018) The Herschel-ATLAS data release 2. Paper II. Catalogs of far-infrared and submillimeter sources in the fields at the south and north Galactic poles. The Astrophysical Journal Supplement Series, 236 (2). 30/1-30/13. ISSN 1538-4365

The Astrophysical Journal Supplement Series, 236:30 (13pp), 2018 June https://doi.org/10.3847/1538-4365/aab8fc

The *Herschel*-ATLAS Data Release 2. Paper II. Catalogs of Far-infrared and Submillimeter Sources in the Fields at the South and North Galactic Poles

S. J. Maddox[1,2], E. Valiante[1], P. Cigan[1], L. Dunne[1,2], S. Eales[1], M. W. L. Smith[1], S. Dye[3], C. Furlanetto[3,4], E. Ibar[5], G. de Zotti[6], J. S. Millard[1], N. Bourne[2], H. L. Gomez[3], R. J. Ivison[2,7], D. Scott[8], and I. Valtchanov[9]
[1] School of Physics and Astronomy, Cardiff University, The Parade, Cardiff CF24 3AA, UK; maddoxs@cardiff.ac.uk
[2] Institute for Astronomy, The University of Edinburgh, Royal Observatory, Blackford Hill, Edinburgh, EH9 3HJ, UK
[3] School of Physics and Astronomy, University of Nottingham, University Park, Nottingham, NG7 2RD, UK
[4] Departamento de Física, Universidade Federale do Rio Grande do Sul., Av. Bento Gonçalves, 9500, 91501-970, Porto Algres, RS, Brazil
[5] Instituto de Física y Astronomía, Universidad de Valparaíso, Avda. Gran Bretaña 1111, Valparaíso, Chile
[6] INAF-Osservatorio Astronomico di Padova, Vicolo dell'Osservatorio 5, I-35122 Padova, Italy
[7] European Southern Observatory, Karl-Schwarzschild-Strasse 2, D-85748, Garching, Germany
[8] Department of Physics & Astronomy, University of British Columbia, 6224 Agricultural Road, Vancouver, BC V6T 1Z1, Canada
[9] Telespazio Vega UK for ESA, European Space Astronomy Centre, Operations Department, E-28691 Villanueva de la Cañada, Spain
Received 2017 December 18; revised 2018 March 18; accepted 2018 March 20; published 2018 May 17

Abstract

The *Herschel* Astrophysical Terahertz Large Area Survey (H-ATLAS) is a survey of 660 deg^2 with the PACS and SPIRE cameras in five photometric bands: 100, 160, 250, 350, and 500 μm. This is the second of three papers describing the data release for the large fields at the south and north Galactic poles (NGP and SGP). In this paper we describe the catalogs of far-infrared and submillimeter sources for the NGP and SGP, which cover 177.1 deg^2 and 303.4 deg^2, respectively. The catalogs contain 118,908 sources for the NGP field and 193,527 sources for the SGP field detected at more than 4σ significance in any of the 250, 350, or 500 μm bands. The source detection is based on the 250 μm map, and we present photometry in all five bands for each source, including aperture photometry for sources known to be extended. The rms positional accuracy for the faintest sources is about 2.4 arcsec in both R.A. and decl. We present a statistical analysis of the catalogs and discuss the practical issues—completeness, reliability, flux boosting, accuracy of positions, accuracy of flux measurements—necessary to use the catalogs for astronomical projects.

Key words: catalogs – cosmology: observations – galaxies: statistics – methods: data analysis – submillimeter: galaxies – surveys

1. Introduction

This is the second of three papers describing the second major data release of the *Herschel* Astrophysical Terahertz Large Area Survey (the *Herschel*-ATLAS or H-ATLAS), the largest single key project carried out in open time with the *Herschel Space Observatory*[10] (Pilbratt et al. 2010). The H-ATLAS is a survey of approximately 660 deg^2 of sky in five photometric bands: 100, 160, 250, 350, and 500 μm (Eales et al. 2010). Although the original goal of the survey was to study dust, and the newly formed stars hidden by dust, in galaxies in the nearby ($z < 0.4$) universe (Dunne et al. 2011; Eales et al. 2018), in practice the exceptional sensitivity of *Herschel*, aided by the large negative *k*-correction at submillimeter wavelengths (Franceschini et al. 1991), has meant that the median redshift of the sources detected in the survey is approximately 1 (Pearson et al. 2013), and our source catalogs include sources up to a redshift of at least 6 (Fudamoto et al. 2017; Zavala et al. 2018).

The five H-ATLAS fields were selected to be areas with relatively little emission from dust in the Milky Way, as judged from the *IRAS* 100 μm images (Neugebauer et al. 1984), and with a large amount of data in other wavebands. In 2010, for the Science Demonstration Phase of *Herschel*, we provided the data products for one 16 deg^2 field in the GAMA 9 hr field (Ibar 2010; Pascale et al. 2011; Rigby et al. 2011; Smith et al. 2011). In our first large data release (DR1), we released the data products for three fields on the celestial equator centered at R.A. of approximately 9, 12, and 15 hr (Valiante et al. 2016; hereafter V16; Bourne et al. 2016), covering a total area of 161 deg^2. These data products included the *Herschel* images in all five bands, a catalog of the 120,230 sources detected in these images and of the 44,835 optical counterparts to these sources.

Our second data release is for the two larger fields at the north and south Galactic poles (NGP and SGP). The NGP field is centered approximately at a R.A. of $13^h\ 18^m$ and a declination of $+29°\ 13'$ (J2000) and has an area of 180.1 deg^2. The NGP field is a roughly square region (Figure 1), and among many other interesting known extragalactic objects, includes the Coma Cluster. The SGP field is centered approximately at a R.A. of $0^h\ 6^m$ and a declination of $-32°\ 44'$ (J2000) and has an area of 317.6 deg^2. The SGP field is elongated in R.A. (Figure 2). Smith et al. 2017, hereafter S17) provide a comprehensive list of the multi-wavelength data that exist for these fields.

Our data release for these fields is described in three papers. In the first paper (S17), we present the images of these fields, including a description of how these images can be used by the astronomical community for a variety of scientific projects. In this paper, we describe the production and properties of the catalogs of far-infrared and submillimeter sources detected in these images. A third paper (Furlanetto et al. 2018, hereafter F18) describes a search for the optical/near-infrared counterparts to the *Herschel* sources in the NGP field and the

[10] *Herschel* is an ESA space observatory with science instruments provided by European-led Principal Investigator consortia and with important participation from NASA.

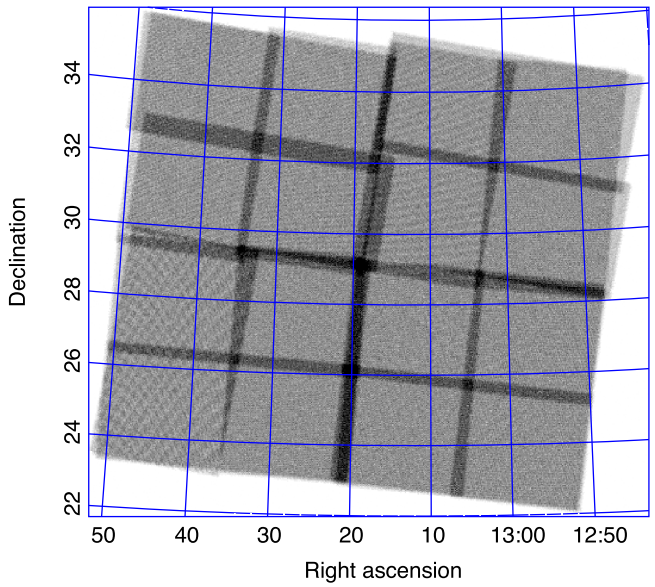

Figure 1. Coverage map for 250 μm observations of the NGP field. The map shows the number of samples from the bolometer timelines contributing to each map pixel, which ranges from 1 to 43, with the median value being 10. The range of the grayscale is from 0 samples (white) to 27 samples (black).

resulting multi-wavelength catalog. The catalogs described in this paper can be obtained from the H-ATLAS website (http://www.h-atlas.org).

The paper is arranged as follows. Section 2 describes the maps and masks used to define the catalogs. Section 3 describes the detection of the sources. Section 4 describes the photometry of the sources. Section 5 describes the catalogs and their properties. Section 6 provides a summary of the paper.

2. Maps, Coverage, and Masks

A detailed description of the processing necessary to produce maps from the *Herschel* raw data is presented in S17. The resulting maps have pixel sizes of 3, 4, 6, 8, and 12 arcsec for 100, 160, 250, 350, and 500 μm, respectively. We chose these to optimally sample the PSF in each band, given that the FWHM of the PSF is 11.4, 13.7, 17.8, 24, and 35.2 arcsec at 100, 160, 250, 350, and 500 μm, respectively. Note that these are different from the canonical pixel sizes used for maps in the *Herschel* Science Archive, which use 3.2, 3.2 6, 10, and 14 arcsec, respectively. The maps made with the PACS camera (100 and 160 μm, Poglitsch et al. 2010) have units of Jy per pixel. The maps made with the SPIRE camera (250, 350, and 500 μm, Griffin et al. 2010) have units of Jy per beam. The beam areas at 250, 350, and 500 μm are 469, 831, and 1804 square arcsec, respectively (Valtchanov 2017). The noise on the images is a combination of instrumental noise and the confusion noise from sources that are too faint to be detected individually. S17 describes a detailed analysis of the noise properties of the images.

The boundary of the mapping data is set by the coverage of the scan lines of the instrument, and thus is very ragged, as shown in Figure 3(a). We define a simple mask to set a clear boundary for the data used in the catalogs; this is mostly restricted to the areas with more than one *Herschel* observation, but does include some areas with only one scan, as can be see in Figure 3(b). The mask reduces the area covered by the catalogs to 177.1 deg^2 and 303.4 deg^2 for the NGP and SGP, respectively. The area covered by the NGP and SGP fields is listed as a function of the number of observations ($N_{\rm scan}$) in Table 1. Within regions where the number of scans is constant, the mean noise is constant, but the noise varies significantly from pixel to pixel, as can be seen in Figure 3(c). This is because the number of detector passes that contribute to a pixel depends on the pixel position relative to the detectors across the scan direction, and also the position relative to the time samples along the scan direction.

The SPIRE and PACS photometers are offset by 21 arcmin, which creates regions around the borders of the survey that are covered by only one of the two photometers. As in previous data releases, we restrict our catalogs to the area covered by the 250 μm maps, so there are some sources that do not have coverage in the PACS 100 and 160 μm bands.

3. Source Detection

3.1. Background Subtraction

Before attempting to detect sources in the maps, we first subtracted a smoothly varying "sky" level to remove the foreground emission from dust in our galaxy, so-called "cirrus emission," and also the emission from clustered extragalactic sources fainter than our detection limit. We used the `nebuliser` function, a program produced by the Cambridge Astronomy Survey Unit to estimate and subtract the sky level on astronomical images.[11] The algorithm first applies a 2D moving box-car median filter to estimate the local sky level for each pixel, and then applies a 2D moving box-car mean filter to slightly smooth the resulting sky map.

The choice of the filter scale used in `nebuliser` is quite critical, since it must be small enough for `nebuliser` to remove small-scale patches of cirrus emission but not so small that the flux from large galaxies is reduced. In practice, for the SPIRE maps we found that a median filter scale of 30 pixels (3 arcmin in the 250 μm band) followed by a linear filter scale of 15 pixels was an acceptable combination.

We tested whether this filtering scale reduced the flux density of extended extragalactic sources by creating simulated maps, placing artificial extended sources on these maps, and then measuring the flux densities of these sources after the application of `nebuliser`. Since the nearby extended galaxies detected by *Herschel* are mostly spiral galaxies, we used truncated exponential profiles for the artificial sources, and convolved these with the SPIRE point-spread function. Previous surveys have found that the observed extent of FIR emission is quite similar to the optical (Smith et al. 2012; Hunt et al. 2015), and the widely used D25 optical diameters for galaxies are roughly equivalent to a distance of five scale lengths from the center of a galaxy, so we truncated the profiles of our artificial submillimeter sources at five scale lengths. At this radius the profile contains 96% of a non-truncated exponential; extending to six scale lengths would increase this to 98%, only a 2% change, so the exact truncation radius is not critical. The resulting diameters ranged from 24 to 192 arcsec. Since the diameters are much larger than the PSF in all of the SPIRE bands, the results will be similar for all bands. The simulations showed that significant flux is lost only for sources that have diameters larger than 3 arcmin, and even for sources above this size, the flux loss is $\lesssim$10%.

[11] http://casu.ast.cam.ac.uk/surveys-projects/software-release/background-filtering

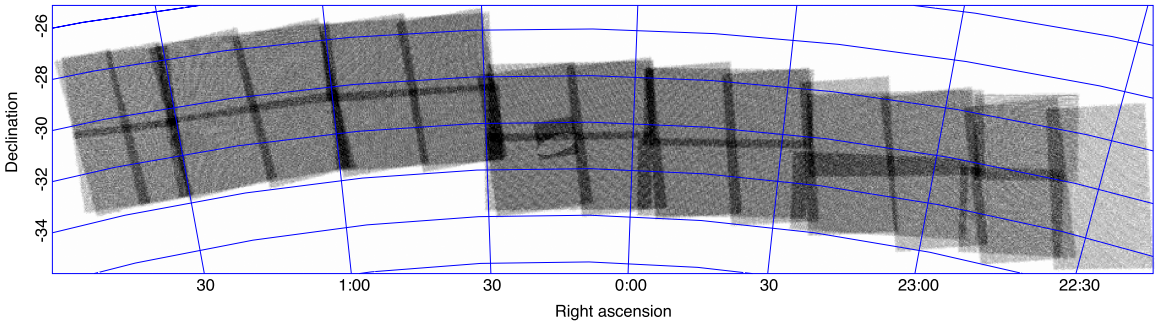

Figure 2. Coverage map for 250 μm observations of the SGP field. The map shows the number of samples from the bolometer timelines contributing to each map pixel, which ranges from 1 to 36, with the median value being 9. The range of the grayscale is from 0 samples (white) to 21 samples (black).

Note that there are only 12 galaxies with diameters larger than 3 arc minutes in the survey: three in the NGP and nine in the SGP. We have made no attempt to correct for any filtering-related flux losses for these galaxies, and recommend users make their own measurements based on the non-filtered maps if more precise extended photometry is required.

We note that the application of `nebuliser` will change the clustering statistics of extragalactic sources. Apart from the foreground cirrus emission, `nebuliser` removes the background produced by the sources that are too faint to be detected individually. This background varies because of the clustering of these faint sources. A source catalog made without any background subtraction will include more sources where this background is high as a result of clusters of these faint sources, so the clustering of the sources in such a catalog will be stronger than in a catalog produced from an image in which this background emission has been removed. An investigation of the clustering in the H-ATLAS catalogs, which includes an analysis of the effect of the subtraction of this background, will be presented by Amvrosiadis et al. (2018, in preparation).

For the PACS maps, the $1/f$-noise from the instrument is much larger than that for SPIRE, making the foreground cirrus emission and the background emission from faint galaxies difficult to detect. Since we could not clearly detect the foreground/background emission on smaller scales, we used a `nebuliser` scale of 5 arcmin.

The raw maps from the SPIRE pipeline have a mean of zero, but the output maps from `nebuliser` have a modal pixel value that is zero. For the SPIRE bands, the instrumental noise is low enough that the flux distribution of detected sources skews the pixel distribution to positive values, so the mean is slightly positive (1.0, 1.0, and 0.6 mJy beam^{-1} at 250, 350, and 500 μm). The PACS detector is less sensitive and less stable than SPIRE, so the instrumental noise dominates over the confusion noise and the pixel distribution is close to Gaussian; the mean of the `nebulised` PACS maps is very close to zero (0.016 MJy sr^{-1}, for both the 100 and 160 μm maps).

3.2. Source Detection

In this section we describe the method used to find the sources on the images. Additional details are given in V16. Sources were detected using the `MADX` algorithm (Maddox et al. 2018, in preparation) applied to the SPIRE maps. `MADX` creates maps of the signal-to-noise ratio and identifies sources by finding peaks in the signal-to-noise. The detection and measurement of fluxes is optimized using a matched filter that is applied to both the signal map and the noise map.

The SPIRE instrumental noise maps are created from the number of detector passes and the estimated instrumental noise per pass, $\sigma_{\rm inst}/\sqrt{N_{\rm sample}}$, as described in S17 and V16.

Since the noise consists of both instrumental noise and confusion noise from the background of undetected sources, we follow the approach of Chapin et al. (2011) to calculate the optimal matched filter in each of the three SPIRE bands. Details of the estimation and form of the matched filter are discussed in V16. The resulting matched filters are slightly more compact than the corresponding PSFs, and have slightly negative regions outside the FWHM.

In the first step of the source detection, peak pixels that have values $>2.5\sigma$ in the filtered 250 μm map are considered as potential sources. We use the 250 μm map since most sources have the highest signal-to-noise in this map. The source position is determined by fitting a Gaussian to the flux densities in the pixels surrounding the pixel containing the peak emission. As an initial estimate of the flux density of the source in each SPIRE band, `MADX` takes the flux density in the pixel closest to the 250 μm position.

The high source density on the SPIRE maps means that these flux estimates often contain contributions from neighboring sources. To mitigate this effect, `MADX` uses the following procedure. In each band, `MADX` sorts the sources in order of decreasing flux density. The flux density of the brightest source is then more precisely estimated using the value of the filtered map interpolated to the exact (sub-pixel) position from the 250 μm map. Using this flux estimate, a point source profile is then subtracted from the map at this position. Since the bright source is now removed from the map, any fainter sources nearby should have fluxes that are not contaminated by the brighter source. The program then moves to the next brightest source and follows the same set of steps.

The point source subtraction continues for all sources in sequence, ordered on the initial flux density estimates. It stops when the PSF for the faintest source is subtracted. The faintest source considered is 2.5σ, based on the initial flux and noise estimates.

If two sources with comparable flux are close to each other, then the algorithm will lead to slightly biased fluxes: the peak of the first source will include some flux from the wings of the second, and be overestimated; the psf-subtracted peak of the second source will have too much subtracted, so the flux will be slightly underestimated. The size of these errors is a steep

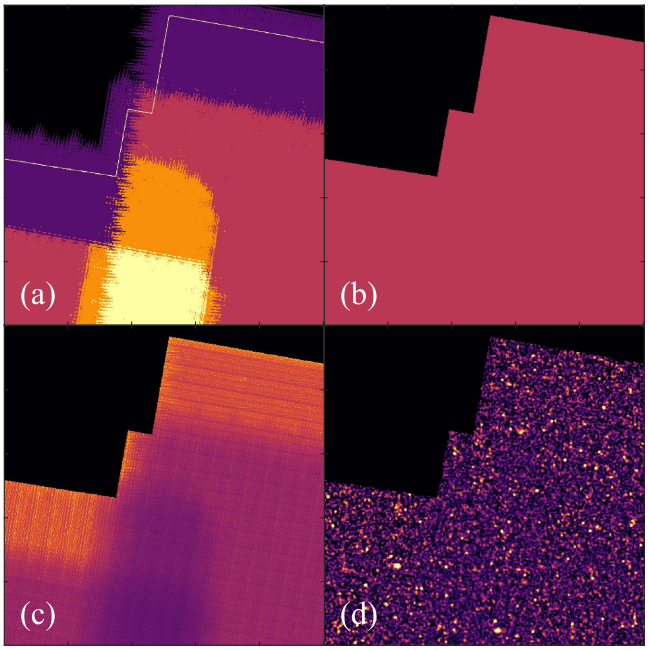

Figure 3. (a) Coverage map for a 50′ × 50′ region of the 250 μm observations, chosen from the NGP field to show the complicated variation in some areas of the survey. The map shows the number of scans covering each pixel, ranging from 1 to 4. The line shows the edge of the masked region retained for the final data. (b) The mask corresponding to the same region. (c) The instrumental noise per pixel for the same region. The average noise varies between regions depending on the number of observing scans: roughly 14 mJy, 10 mJy, 8 mJy, and 7 mJy for the 1, 2, 3, and 4 $N_{\rm scan}$ regions, respectively. Also note that the noise varies significantly within regions where the number of scans is constant. This is due to the variation in the number of detector passes across a single scan of the instrument, and the pixel position relative to the time samples along the scan direction. (d) The 250 μm data for the same region.

Table 1
Area of the Survey Data in deg^2, as a Function of the Number of *Herschel* Observations ($N_{\rm scan}$)

	$N_{\rm scan}$							
	1	2	3	4	5	6	7	Total
NGP total	8.3	139.3	26.2	5.7	0.4	0.2	0.1	180.1
NGP+mask	5.5	139.1	26.2	5.7	0.4	0.2	0.1	177.1
SGP total	43.0	210.2	52.2	11.1	0.7	0.2	0	317.6
SGP+mask	30.5	208.7	52.1	11.1	0.7	0.2	0	303.4

Note. The entries with "total" show all of the observed area. The entries with "+mask" are the areas within the mask used to define the catalog.

function of the separation of two sources. For a roughly Gaussian PSF, and two equal sources separated by twice the FWHM, the first source will have a flux overestimated by a factor 1.06 and the second will be underestimated by 0.997. If they are separated by the FWHM, then the first source is overestimated by a factor of 1.5, and the second is underestimated by a factor of 0.75. At such a small separation, the images are strongly blended, so a more sophisticated deblending algorithm would be required to improve the flux estimates. For our maps the instrumental noise is comparable to the confusion noise, so there is only a small potential gain from reducing this source of confusion noise. The error analysis presented in V16 is based on simulated catalogs that use the deblending as described above, so the quoted errors include the average deblending errors.

One consequence of these steps is that some sources will have final 250 μm flux densities that are less than the original 2.5σ cut. Also, most sources are brighter at 250 μm than at the two longer wavelengths, so the estimates of the flux densities in the 350 and 500 μm bands are typically significantly lower in signal-to-noise, and can be negative. Note that a negative flux measurement is perfectly reasonable as long as the associated error is comparable.

The released catalog contains only sources detected at more than 4σ significance in any of the bands. At 4σ, we feel confident that every catalog entry corresponds to a real astrophysical source. We present flux measurements for all of the bands for these sources, even if the measurements are negative. We retain these negative measurements so that the distribution of fluxes in the catalogs is consistent with the errors, and not truncated at an arbitrary limit; we do not report "upper limits."

4. Photometry

4.1. Point Sources

4.1.1. SPIRE

V16 carried out extensive simulations to determine the errors on flux density estimates for point sources in the GAMA fields. The data for the NGP and SGP fields were taken in the same mode with the same observing strategy as the data for the GAMA fields presented by V16. This means that the statistical properties of the data are essentially identical to the V16 maps, so we can directly apply the V16 results to our current data. The only potential difference is that the current maps have some areas where the total coverage has more than four observations, which was the maximum coverage in V16. As shown in Table 1, the area with $N_{\rm scan} > 4$ corresponds to less than 0.5% of the total, and thus makes a negligible difference to the overall statistics of the catalog.

V16 followed the simple procedure of injecting artificial sources of known flux density into the real maps and then using MADX to estimate their flux densities (Section 3.2). They found that at 250 μm, the detection wavelength, the confusion noise varies as a function of source flux density, and gave a simple formula to approximate this:

$$\sigma_{\rm con250} = \sqrt{\min\left(0.0049, f_{250}/5.6\right)^2 + 0.00253^2} \ \ {\rm Jy}. \quad (1)$$

They found that at 350 and 500 μm the confusion noise is roughly constant, with $\sigma_{\rm con350} = 0.00659$ Jy and $\sigma_{\rm con500} = 0.00662$ Jy.

We combine the instrumental and confusion noise to estimate the flux uncertainty for each individual source: we used these formulae to estimate the confusion noise at the flux level of the source; we used the maps of the instrumental noise (Section 2) to estimate the instrumental noise at the position of the source; and then added the confusion and instrumental noise in quadrature to give the total flux uncertainty for the source.

Our strategy of creating the H-ATLAS survey from overlapping tiles (S17) means that the instrumental noise varies systematically between different areas of the maps. Figure 4 shows histograms of instrumental noise and total noise (instrumental noise plus confusion noise) for all pixels and at the positions of all sources. The multiple peaks are the results of our tiling strategy. The main peak corresponds to

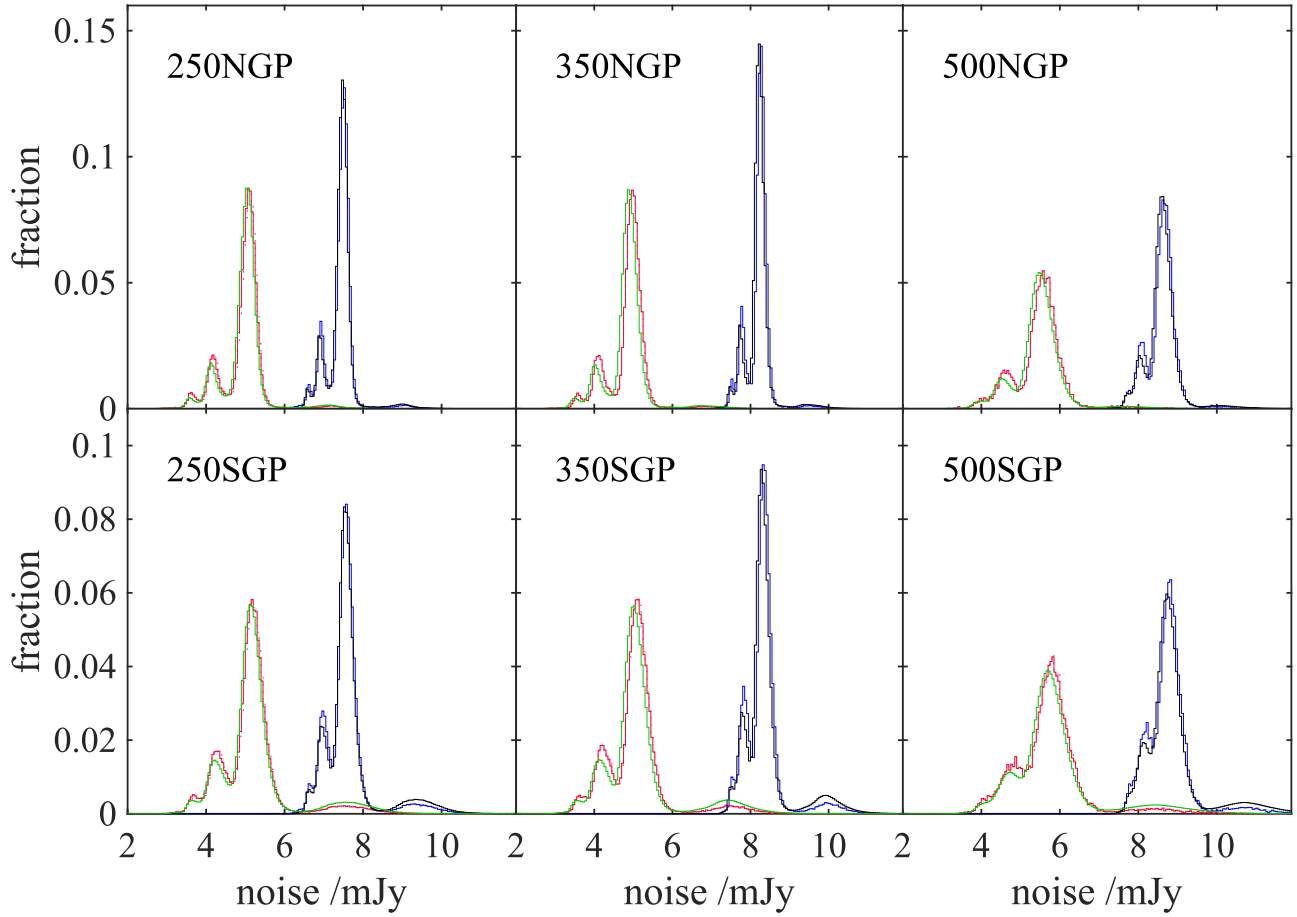

Figure 4. The distribution of instrumental and total noise for the 250, 350, and 500 μm bands for the NGP and SGP fields. Green represents the instrumental noise and black represents the total noise for all pixels; red represents the instrumental noise and blue represents the total noise at the positions of all sources. The multiple peaks are the results of our tiling strategy. The main peak corresponds to the large fraction of the survey area that was covered by two individual *Herschel* observations (S17). The smaller peaks correspond to the small fraction of the survey area that was either covered by more than two observations, or, in the case of one end of the SGP (S17), a single observation (the small peak at the right in the bottom panels.

the large fraction of the survey area that was covered by two individual *Herschel* observations (S17). The smaller peaks at lower noise correspond to the smaller fraction of the survey area that was covered by more than two observations. The small peak at higher noise in the SGP field corresponds to the area at the western end that was covered by a single observation (S17).

The variation of noise across the maps means that the 4σ flux density limit varies over the fields, and hence the available area depends on the chosen flux density limit. Figure 5 shows the relationship between area and flux density limit for each of the H-ATLAS fields, including the GAMA fields.

4.1.2. PACS

As in V16, we used aperture photometry to estimate the flux densities in the two PACS bands. We did this for two reasons. First, the PACS PSF for our observing mode (fast-parallel scan mode) is not well determined near its peak (see V16 and S17 for extensive discussions). Second, if we estimated the 100 and 160 μm flux densities at the 250 μm position, as we did for the 350 and 500 μm bands, we would likely significantly underestimate the flux density, because of the higher resolution of the PACS maps.

V16 describes an extensive investigation of the optimum aperture size, and we follow that paper in using an aperture with a radius equal to the FWHM, which is 11.4 arcsec for 100 μm and 13.7 arcsec for 160 μm. Although the "sky" level has already been subtracted with `nebuliser`, we subtracted the mean value from each image before carrying out the photometry, to ensure that the statistical properties of the sources in the catalogs are not affected by any residual errors in the sky subtraction. To provide an accurate treatment of the contribution from fractional pixels near aperture boundaries, we divided each pixel into 16, and assigned one-sixteenth of the flux density in each sub-pixel, corresponding to a nearest-pixel interpolation. Then the flux density from each sub-pixel that lies within the aperture is added together to produce the total aperture flux. We also tried bilinear, and bicubic interpolation methods and found negligible differences in the resulting aperture fluxes. Since only $\simeq$10% of the SPIRE sources were clearly detected on the PACS images, we centered the aperture on the 250 μm position.

We corrected the aperture flux densities to total flux densities using the table of the encircled energy fraction (EEF) described in V16 and available at http://www.h-atlas.org/. We made a further correction to allow for the effect of the errors on the 250 μm positions, since any error in the position will lead to the small PACS apertures missing flux. V16 describes simulations of this effect, and we follow that paper in compensating for this

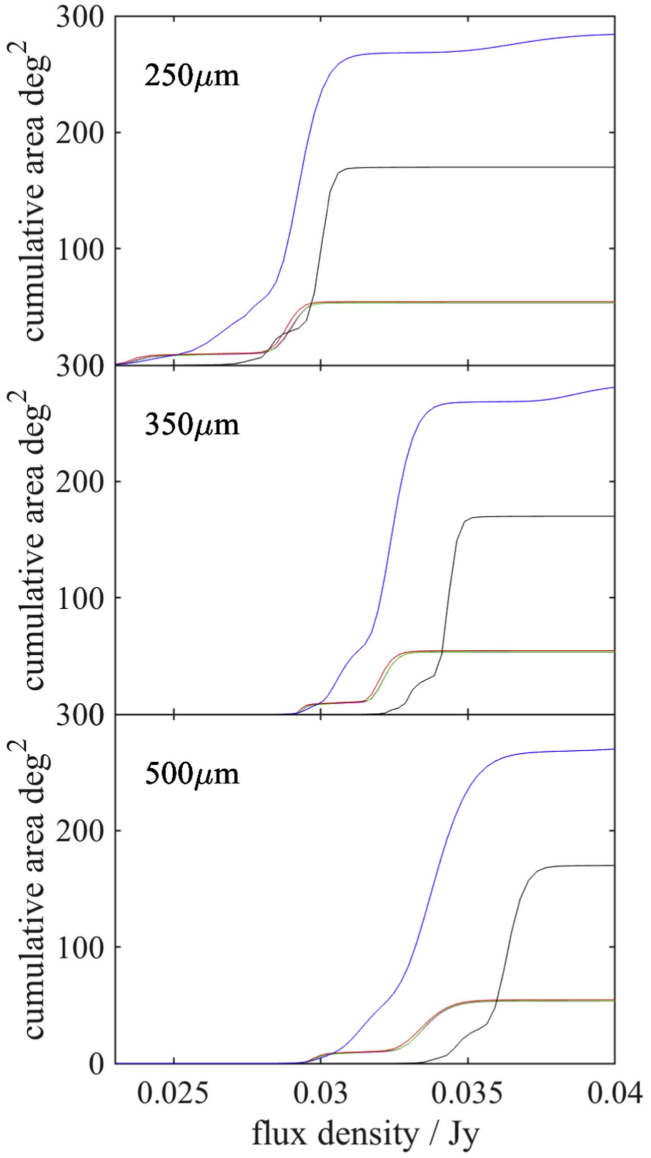

Figure 5. Relationship between area and 4σ flux density limit for the H-ATLAS fields: NGP—black; SGP—blue; GAMA9—magenta; GAMA12—green and GAMA15—cyan. The more sensitive areas correspond to the tile overlaps in each field. The westerly end of SGP has only a single SPIRE observation, which explains the kink at high flux densities in the blue line in these panels.

effect by multiplying the flux densities by 1.1 and 1.05 at 100 and 160 μm, respectively.

We describe how we estimated the errors on these flux estimates in the following subsection.

4.2. Extended Sources

The approach in Section 4.1 gives optimal flux density estimates for point sources, but will substantially underestimate the flux density of extended sources. As in V16, we used the *r*-band sizes of optical counterparts to the *Herschel* sources to indicate which sources are likely to require aperture photometry rather than the methods described in the last section. We followed different methods for the NGP and the SGP because of the lack of a comprehensive identification analysis for the SGP. We estimate aperture photometry for extended sources in both PACS and SPIRE bands.

4.2.1. The NGP

In the NGP, F18 carried out a search for optical counterparts to the *Herschel* sources on the *r*-band images of the Sloan Digital Sky Survey (SDSS), which was almost exactly the same as that carried out by Bourne et al. (2016) for the H-ATLAS GAMA fields. Our initial list of NGP sources that might require aperture photometry were the sources with optical identifications with reliability $R > 0.8$ from F18.

In our previous data release (V16) we calculated the sizes of our apertures from the SDSS parameter `isoA_r`, which was available in SDSS DR7. However, this parameter was not available in SDSS DR10, on which F18 based their analysis. After an investigation of the various size measurements available in DR10, we found that the parameter `petroR90_r`, the 90% Petrosian radius met our needs since there is a simple scaling between it and `isoA_r`, with `isoA_r` $\simeq 1.156$ `petroR90_r`. The scale-factor 1.156 is derived from a simple fit to `isoA_r` as a function of `petroR90_r`.

We considered that for H-ATLAS sources with optical counterparts with `petroR90_r` less than 8.6 arcsec (equivalent to the value of `isoA_r` of 10 arcsec used in V16), the source is still unlikely to be extended in the SPIRE bands, and for these H-ATLAS sources we preferred to adopt the flux densities in the SPIRE bands produced by `MADX` (Section 4.1.1). However, if the H-ATLAS source had an optical counterpart with `petroR90_r` greater than 8.6 arcsec, we measured aperture photometry for the SPIRE bands. We calculated the radius of the aperture using the same formula as V16 (with `isoA_r` replaced by `petroR90_r`):

$$r_{\rm ap} = \sqrt{\texttt{FWHM}^2 + (1.156\ \texttt{petroR90\_r})^2}\,, \qquad (2)$$

where `FWHM` is the FWHM of the point-spread function for the passband being measured, and all radii are measured in arcseconds. As discussed above (Section 4.1.2), we also use aperture photometry in the PACS bands for sources without reliable optical counterparts, using an aperture with a radius equal to the FWHM.

After calculating the aperture using Equation (2), we visually compared it with the 250 μm emission from the source, since in some cases the aperture is not well-matched to the 250 μm emission, either being too small, too large, with the wrong shape or including the flux from a neighboring galaxy (see V16 for examples). In these cases, we chose a more appropriate aperture for the galaxy, which may involve changing the radius or changing to an elliptical aperture. We also visually inspected the 3000 sources with the brightest 250 μm flux densities from `MADX` in order to check whether there were any obvious additional extended sources. For these sources, too, we chose appropriate apertures to include all of the emission. In total, for the NGP there are 77 of these "customized apertures." The semimajor, semiminor axes, and position angles of these customized apertures are given as part of the data release.

We centered the apertures on the optical positions, since these are more accurately determined than the *Herschel* positions. Although the "sky" level on both the PACS and SPIRE images has already been subtracted with `nebuliser`, we subtracted the mean value from each image before carrying out the photometry, in order to avoid residual errors in the sky subtraction affecting the statistical properties of the catalogs. As described in Section 4.1.2, we divided each pixel into 16, assigning one-sixteenth of the flux density in each sub-pixel,

and added up the flux density in each sub-pixel within the aperture. We corrected the PACS flux densities to total flux densities using the table EEF described in V16 and available at http://www.h-atlas.org/. We corrected all the SPIRE aperture flux densities for the fraction of the PSF outside the aperture using a table of corrections determined from the best estimate of the SPIRE PSF (Griffin et al. 2013; Valtchanov 2017), which is provided as part of the data release (see V16 for more details).

We calculated errors in the aperture flux densities from the results of the Monte Carlo simulation of S17. S17 placed apertures randomly on the SGP and NGP maps in areas that are made from two individual observations ($N_{\rm scan} = 2$), varying the aperture radii from approximately the beam size up to 100 arcsec in 2 arcsec intervals and using 3000 random positions for each aperture radius. They found that the error, $\sigma_{\rm ap}$ in mJy, depends on the radius the aperture as a double power law:

$$\sigma_{\rm ap}({\rm mJy}) = \begin{cases} Ar^{\alpha}, & \text{if } r \leqslant 50'', \\ B(r-50)^{\beta} + A50^{\alpha}, & \text{for } r > 50''. \end{cases} \quad (3)$$

The constants A, B, α, and β are given in Table 3 of S17. We used this equation for the sources on parts of the images made from two observations. In parts of the images made from more than two observations there is less instrumental noise; for sources in these more sensitive parts of the images we used the extensions of Equation (3) derived by S17; i.e., Equation (4) in S17 for SPIRE and Equation (6) in S17 for PACS. Note that this procedure for estimating uncertainties intrinsically includes confusion noise and any correlated errors in the map data.

Finally, we only used the aperture flux density if it is significantly larger than the point source estimate, i.e.,

$$F_{\rm ap} - F_{\rm ps} > \sqrt{\sigma_{\rm ap}^2 - \sigma_{\rm ps}^2}. \quad (4)$$

In summary, of the 118,986 sources in the NGP, we measured aperture flux densities at 250 μm for 889 sources.

4.2.2. The SGP

For the SGP area no SDSS data exist and we have not carried out the comprehensive identification analysis that we performed for the other four fields. Instead, we have carried out a rudimentary identification analysis using the 2MASS survey (Skrutskie et al. 2006). We first found a 2MASS galaxy parameter that provides a useful estimate of the size of the galaxy. We found that the 2MASS parameter "super-coadd 3-σ isophotal semimajor axis," `sup_r_3sig`, has a simple scaling with the `isoA_r`: `isoA_r` $\simeq$ 1.96 `sup_r_3sig`. The scale-factor 1.96 is derived from a simple fit to `isoA_r` as a function of `sup_r_3sig`.

We found all 2MASS galaxies in the SGP region with `sup_r_3sig` > 5.1 arcsec, equivalent to `isoA_r` $=$ 10 arcsec. There are 6249 of these galaxies. We then found all H-ATLAS sources in the SGP within 5 arcsec of a 2MASS galaxy. There are 3444 of these sources. We used the surface density of *Herschel* sources to estimate the probability of a *Herschel* source falling within 5 arcsec of a 2MASS galaxy by chance; we estimate that only 23 (0.7%) of these matches should not be physical associations of the H-ATLAS source and the 2MASS galaxy.

For these sources, we calculated the radius of the aperture to use for photometry using the relationship:

$$r_{\rm ap} = \sqrt{{\rm FWHM}^2 + (1.96\ {\rm sup\_r\_3sig})^2}\,. \quad (5)$$

This is the same as Equation (2), except for the change in the parameter used to estimate the size of the galaxy. In principle we could use `sup_r_3sig` as our radius measure for the sources in the NGP, but SDSS is significantly deeper than 2MASS so the measurements are likely to have smaller uncertainties.

As for the NGP, we then visually compared the apertures with the 250 μm emission from the source, modifying the aperture when necessary (see above). We also visually inspected the 5000 sources with the brightest 250 μm flux densities from `MADX` in order to check whether there were any obvious additional extended sources. For these sources, we also chose appropriate apertures to include all of the emission. In total, for the SGP there are 142 customized apertures, for which the details are given as part of the data release.

In the case of the SGP, we centered the apertures on the 250 μm positions rather than on the optical positions. Otherwise we followed exactly the same procedures to estimate the fluxes and errors as for the NGP, described in Section Section 4.1.2. In summary, of the 118,986 sources in the SGP, we measured aperture flux densities at 250 μm for 1452 sources.

4.3. Comparison to Planck Photometry

Estimating the flux density of extended sources is sensitive to the background subtraction and choice of aperture size, so it is useful to compare our extended source fluxes to other available measurements. In particular, for the 350 μm and 500 μm bands, we have compared to the compact source catalog from the *Planck*[12] survey (Planck Collaboration XXVI 2016). Given the low-surface density of sources, a simple positional match is sufficient to cross-identify sources in common. We find 32 matches in the NGP, and 42 in the SGP as listed in Table 2 and plotted in Figure 6. Most sources, 49/74, are large enough that we had visually inspected them and assigned custom apertures (see Sections 3.2.1 and 3.2.2), 21 are extended and have automatically assigned apertures, and 4 are point sources. We have adopted the *Planck* APERFLUX photometry as recommended by Planck Collaboration XXVI (2016) for these wavelengths. The *Planck* 545 GHz (550 μm) flux densities, and their errors, have been scaled up by a factor of 1.35 to convert them to 500 μm.

As seen in Figure 6, there is a very good correspondence between the measurements with no significant systematic offsets or nonlinearity. The *Planck* fluxes do appear to be slightly higher than the H-ATLAS fluxes at less than 1 Jy, but summing over all sources, the offset is less than the 2σ significance level. It is likely that this is a result of flux boosting in the *Planck* catalog: if the *Planck* fluxes were each shifted lower by half of their quoted uncertainty, there would be no offset. After shifting to remove the offset, the scatter between the measurements is consistent with the quoted uncertainties, with $\chi^2 = 71$ and 72 degrees of freedom.

[12] *Planck* (http://www.esa.int/Planck) is an ESA science mission with instruments and contributions directly funded by ESA Member States, NASA, and Canada.

Table 2
Comparison of H-ATLAS with *Planck* Flux Densities (Jy, Rounded to 1 mJy) at 350 and 500 μm

HATLAS_IAU_ID	F350BEST	$F_{\rm Planck350}$	F500BEST	$F_{\rm Planck500}$
HATLAS J125026.0+252947	12.128 ± 2.696	12.128 ± 2.696	5.208 ± 1.160	5.666 ± 0.393
HATLAS J125440.7+285619	4.974 ± 0.285	5.254 ± 0.204	1.678 ± 0.126	1.836 ± 0.176
HATLAS J131136.9+225454	3.469 ± 0.304	3.684 ± 0.265	1.279 ± 0.134	1.328 ± 0.161
HATLAS J132035.3+340824	2.255 ± 0.009	2.199 ± 0.270	0.715 ± 0.009	0.869 ± 0.200
HATLAS J133955.6+282402	1.701 ± 0.131	1.563 ± 0.181	0.570 ± 0.061	0.471 ± 0.130
HATLAS J125144.9+254615	1.589 ± 0.215	1.740 ± 0.154	0.639 ± 0.096	0.842 ± 0.176
HATLAS J131503.5+243709	1.588 ± 0.008	2.101 ± 0.298	0.544 ± 0.009	0.976 ± 0.207
HATLAS J133457.2+340238	1.311 ± 0.108	1.454 ± 0.271	0.444 ± 0.051	0.424 ± 0.275
HATLAS J125253.6+282216	1.168 ± 0.099	0.985 ± 0.142	0.359 ± 0.008	0.512 ± 0.157
HATLAS J132815.2+320157	1.043 ± 0.093	1.022 ± 0.280	0.362 ± 0.044	···
HATLAS J134308.8+302016	1.032 ± 0.114	0.605 ± 0.288	0.319 ± 0.009	···
HATLAS J131206.6+240543	1.019 ± 0.029	1.444 ± 0.278	0.385 ± 0.020	···
HATLAS J132255.7+265857	0.987 ± 0.094	0.958 ± 0.228	0.330 ± 0.045	···
HATLAS J131612.2+305702	0.925 ± 0.117	1.498 ± 0.310	0.346 ± 0.055	···
HATLAS J130547.6+274405	0.922 ± 0.118	1.278 ± 0.442	0.363 ± 0.055	0.760 ± 0.292
HATLAS J130514.1+315959	0.832 ± 0.104	0.840 ± 0.165	0.258 ± 0.008	···
HATLAS J130056.1+274727	0.769 ± 0.023	0.934 ± 0.269	0.268 ± 0.018	···
HATLAS J133026.1+313707	0.737 ± 0.100	0.861 ± 0.220	0.267 ± 0.047	···
HATLAS J124610.1+304355	0.718 ± 0.047	0.525 ± 0.342	0.241 ± 0.009	···
HATLAS J130125.2+291849	0.701 ± 0.008	0.854 ± 0.233	0.232 ± 0.009	···
HATLAS J130947.5+285424	0.680 ± 0.122	0.971 ± 0.168	0.220 ± 0.057	···
HATLAS J130617.2+290346	0.675 ± 0.103	1.057 ± 0.288	0.247 ± 0.049	···
HATLAS J131241.9+224950	0.650 ± 0.154	0.230 ± 0.209	0.253 ± 0.072	···
HATLAS J131101.7+293442	0.628 ± 0.089	1.114 ± 0.409	0.189 ± 0.008	···
HATLAS J125108.4+284705	0.611 ± 0.090	0.661 ± 0.285	0.245 ± 0.043	···
HATLAS J133550.1+345957	0.602 ± 0.025	1.056 ± 0.236	0.200 ± 0.019	···
HATLAS J132948.2+310748	0.559 ± 0.017	0.580 ± 0.308	0.190 ± 0.014	···
HATLAS J131730.6+310533	0.548 ± 0.021	0.610 ± 0.253	0.196 ± 0.016	···
HATLAS J131327.0+274807	0.520 ± 0.114	1.149 ± 0.379	0.195 ± 0.053	···
HATLAS J133554.6+353511	0.510 ± 0.079	0.925 ± 0.148	0.187 ± 0.038	···
HATLAS J125008.7+330933	0.509 ± 0.022	0.521 ± 0.209	0.190 ± 0.017	···
HATLAS J131745.2+273411	0.500 ± 0.019	1.178 ± 0.230	0.169 ± 0.015	···
HATLAS J235749.9−323526	24.881 ± 1.894	24.513 ± 0.723	10.667 ± 0.821	11.743 ± 0.566
HATLAS J003024.0−331419	22.390 ± 1.140	23.014 ± 0.447	8.103 ± 0.497	8.624 ± 0.243
HATLAS J013418.2−292506	17.557 ± 1.040	16.747 ± 3.56	5.931 ± 0.452	5.979 ± 0.202
HATLAS J005242.2−311222	4.922 ± 0.445	6.425 ± 0.225	1.788 ± 0.198	2.892 ± 0.220
HATLAS J003415.3−274812	4.063 ± 0.407	4.183 ± 0.341	1.482 ± 0.180	1.705 ± 0.181
HATLAS J234751.7−303118	3.420 ± 0.433	3.317 ± 0.170	1.288 ± 0.192	1.386 ± 0.212
HATLAS J225801.7−334432	3.294 ± 0.225	3.627 ± 0.266	1.149 ± 0.102	1.404 ± 0.173
HATLAS J003658.8−292839	2.246 ± 0.009	2.486 ± 0.382	0.741 ± 0.009	0.601 ± 0.227
HATLAS J224218.1−300333	1.963 ± 0.312	1.768 ± 0.184	0.869 ± 0.140	0.629 ± 0.217
HATLAS J011407.0−323908	1.622 ± 0.123	2.097 ± 0.507	0.629 ± 0.058	0.763 ± 0.327
HATLAS J000833.7−335147	1.533 ± 0.235	1.322 ± 0.309	0.504 ± 0.107	···
HATLAS J222421.6−334139	1.519 ± 0.043	1.819 ± 0.156	0.481 ± 0.031	0.953 ± 0.151
HATLAS J013906.2−295457	1.445 ± 0.034	2.064 ± 0.374	0.545 ± 0.024	0.803 ± 0.231
HATLAS J011035.6−301316	1.314 ± 0.035	1.482 ± 0.180	0.497 ± 0.025	0.536 ± 0.216
HATLAS J222521.1−312116	1.251 ± 0.120	1.551 ± 0.294	0.480 ± 0.058	···
HATLAS J014021.4−285445	1.224 ± 0.093	···	0.421 ± 0.455	0.990 ± 0.259
HATLAS J013150.3−330710	1.192 ± 0.118	2.073 ± 0.308	0.397 ± 0.056	0.983 ± 0.198
HATLAS J010612.2−301041	1.150 ± 0.131	1.074 ± 0.294	0.388 ± 0.062	···
HATLAS J014744.6−333607	1.089 ± 0.035	1.060 ± 0.287	0.365 ± 0.025	···
HATLAS J005747.0−273004	1.073 ± 0.032	2.043 ± 0.560	0.445 ± 0.023	1.118 ± 0.258
HATLAS J010456.0−272545	1.035 ± 0.032	1.364 ± 0.266	0.365 ± 0.023	···
HATLAS J225956.7−341415	1.033 ± 0.118	1.218 ± 0.267	0.314 ± 0.009	···
HATLAS J011101.1−302620	0.997 ± 0.033	0.770 ± 0.182	0.362 ± 0.024	···
HATLAS J222610.7−310840	0.956 ± 0.093	0.621 ± 0.349	0.342 ± 0.046	···
HATLAS J011429.7−311053	0.917 ± 0.114	1.069 ± 0.280	0.331 ± 0.054	···
HATLAS J012658.0−323234	0.845 ± 0.097	0.982 ± 0.341	0.296 ± 0.046	···
HATLAS J012315.0−325028	0.806 ± 0.031	0.744 ± 0.465	0.277 ± 0.023	···
HATLAS J002354.3−323210	0.803 ± 0.030	1.108 ± 0.193	0.314 ± 0.022	···
HATLAS J002938.2−331534	0.745 ± 0.111	0.747 ± 0.363	0.296 ± 0.052	···
HATLAS J011122.3−291404	0.727 ± 0.031	1.547 ± 0.455	0.278 ± 0.022	···
HATLAS J005457.3−320115	0.719 ± 0.008	0.780 ± 0.258	0.245 ± 0.009	···
HATLAS J012434.5−331024	0.640 ± 0.030	0.946 ± 0.288	0.204 ± 0.022	···

Table 2
(Continued)

HATLAS_IAU_ID	F350BEST	$F_{\rm Planck350}$	F500BEST	$F_{\rm Planck500}$
HATLAS J230549.0−303642	0.637 ± 0.085	0.868 ± 0.345	0.191 ± 0.009	···
HATLAS J000254.5−341407	0.572 ± 0.026	1.160 ± 0.409	0.207 ± 0.020	···
HATLAS J001112.7−333442	0.499 ± 0.036	0.555 ± 0.221	0.171 ± 0.026	···
HATLAS J003651.4−282200	0.466 ± 0.065	0.438 ± 0.324	0.162 ± 0.032	···
HATLAS J010723.3−324943	0.448 ± 0.047	0.839 ± 0.881	0.141 ± 0.009	···
HATLAS J225739.6−293730	0.433 ± 0.009	0.975 ± 0.293	0.292 ± 0.009	···
HATLAS J004806.7−284818	0.407 ± 0.008	0.069 ± 0.238	0.126 ± 0.009	···
HATLAS J235939.7−342829	0.352 ± 0.064	0.733 ± 0.215	0.095 ± 0.009	···
HATLAS J005852.3−281812	0.349 ± 0.019	0.209 ± 0.490	0.113 ± 0.015	···
HATLAS J233007.0−310738	0.213 ± 0.040	0.433 ± 0.305	0.101 ± 0.022	···

Note. We have adopted the *Planck* APERFLUX photometry as recommended by Planck Collaboration XXVI (2016) for these wavelengths. *Planck* 545 GHz (550 μm) flux densities, and their errors, have been scaled up by a factor of 1.35 to convert them to 500 μm.

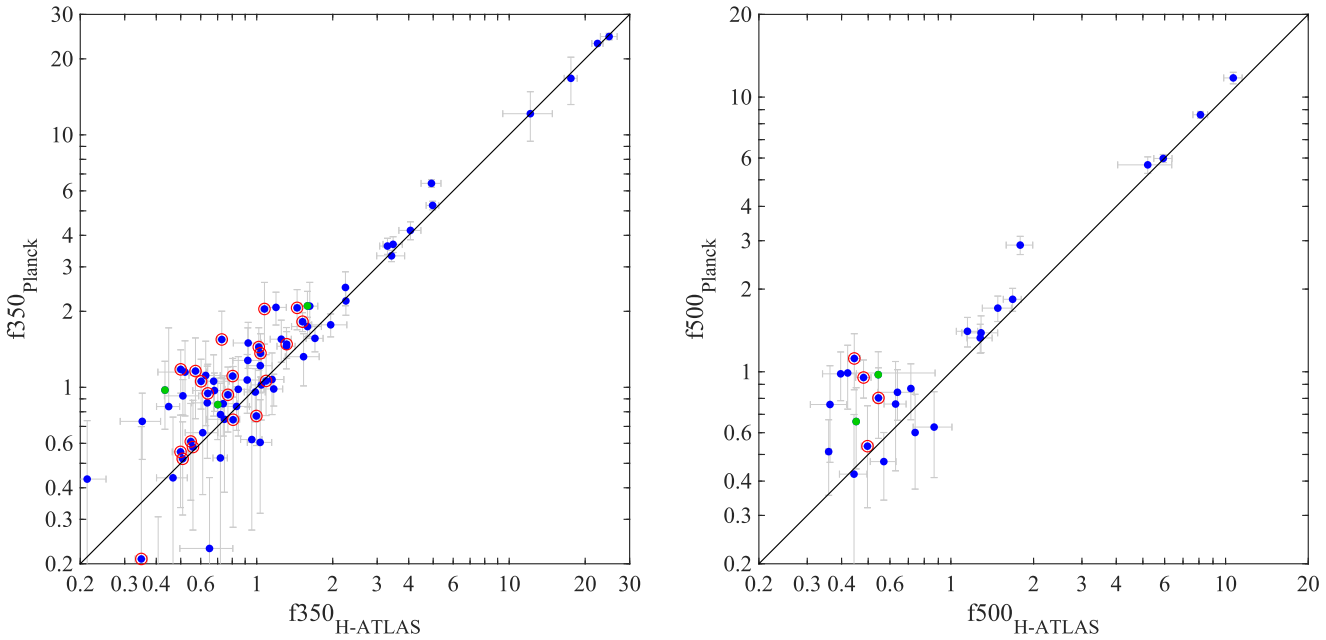

Figure 6. Comparison between H-ATLAS and *Planck* flux density measurements for the 350 and 500 μm bands. Green points are H-ATLAS point sources; blue points are H-ATLAS extended sources; extended sources that have *not* been given a custom aperture are circled in red. The majority of the *Planck* sources are so large that they have been given custom apertures in the H-ATLAS catalog: 48/73 at 350 μm; and 21/27 at 500 μm.

Planck Collaboration XXVI (2016) quoted 90% completeness limits of 791 mJy and 555 mJy for the 350 and 550 μm catalogs, respectively. The comparison with the H-ATLAS catalog suggests 90% completeness down to F350BEST= 650 mJy. For the Planck 550 μm catalog, the quoted 90% completeness limit of 555 mJy corresponds to 749 mJy at 500 μm; the comparison with the H-ATLAS catalog suggests 90% completeness down to F500BEST=400 mJy. Despite the relatively small number of sources, our comparison suggests that the quoted Planck limits are quite conservative.

4.4. Color Corrections and Flux Calibration

The large wavelength range within each of the SPIRE pass bands means that both the size of the PSF and the power detected by SPIRE depend on the spectral energy distribution of the source. The SPIRE data-reduction pipeline and ultimately our flux densities are based on the assumption that the flux density of a source varies with frequency as ν^{-1}. If the user knows the SED of a source, the flux densities should be corrected using corrections from either table 5.7 or 5.8 from the SPIRE handbook[13] (Valtchanov 2017). It is important to apply these corrections, since they can be quite large: for a point source with a typical dust spectrum ($T = 20$ K, $\beta = 2$), the multiplicative corrections are 0.96, 0.94, and 0.90 at 250, 350, and 500 μm, respectively. The catalog fluxes have had no color correction applied.

As with SPIRE, the PACS flux densities are also based on the assumption that the flux density of the source is proportional to ν^{-1}, and a correction is required for sources that follow a different SED. The required corrections are described in the PACS Color-Correction document.[14]

On top of all other errors, there is an additional error due to the uncertain photometric calibration of *Herschel*. As in V16, we assume conservative calibration errors of 5.5% for the three

[13] http://herschel.esac.esa.int/Docs/SPIRE/spire_handbook.pdf
[14] http://herschel.esac.esa.int/twiki/pub/Public/PacsCalibrationWeb/cc_report_v1.pdf

Table 3
Data Columns in the H-ATLAS Catalog Files

Column Name	Description
HATLAS_IAU_ID	Source name using the IAU standard
IDNAME	Internal catalog name based on the source number and field name
R.A.	R.A. in degrees based on the H-ATLAS data
Decl.	Decl. in degrees based on the H-ATLAS data
F250	Point source 250 μm flux estimate in Jy
F350	Point source 350 μm flux estimate in Jy
F500	Point source 500 μm flux estimate in Jy
E250	Uncertainty on point source 250 μm flux in Jy (includes both confusion and instrumental noise)
E350	Uncertainty on point source 350 μm flux in Jy (includes both confusion and instrumental noise)
E500	Uncertainty on point source 500 μm flux in Jy (includes both confusion and instrumental noise)
F250BEST	Best estimate of 250 μm flux in Jy: point source if unresolved; aperture flux if resolved.
E250BEST	Uncertainty on best estimate 250 μm flux in Jy (includes both confusion and instrumental noise)
AP250	Semimajor axis of 250 μm band aperture in arcsecs. -99 if point source flux used.
F350BEST	Best estimate of 350 μm flux in Jy: point source if unresolved; aperture flux if resolved.
E350BEST	Uncertainty on best estimate 350 μm flux in Jy (includes both confusion and instrumental noise)
AP350	Semimajor axis of 350 μm band aperture in arcsecs. -99 if point source flux used
F500BEST	Best estimate of 500 μm flux in Jy: point source if unresolved; aperture flux if resolved.
E500BEST	Uncertainty on best estimate 500 μm flux in Jy (includes both confusion and instrumental noise)
AP500	Semimajor axis of 350 μm band aperture in arcsecs. -99 if point source flux used
F100BEST	Best estimate of 100 μm flux in Jy. The value -1 indicates that there is no PACS coverage for the source
E100BEST	Uncertainty on 100 μm flux in Jy. The value -1 indicates that there is no PACS coverage for the source
AP100	Semimajor axis of aperture used for 100 μm flux, in arcsecs.
F160BEST	Best estimate of 160 μm flux in Jy. The value -1 indicates that there is no PACS coverage for the source
E160BEST	Uncertainty on 160 μm flux in Jy. The value -1 indicates that there is no PACS coverage for the source
AP160	Semimajor axis of aperture used for 160 μm flux, in arcsecs.
AP_RMIN	Semiminor axis of aperture in arcsecs. Set only for custom apertures. The value -99 flags that either an automatically calculated circular aperture has been used, or no aperture has been used.
AP_PA	Position angle of major axis of aperture in degrees anti-clockwise from west. Set only for custom apertures. The value -99 flags that either an automatically calculated circular aperture has been used, or no aperture has been used

Note. For NGP sources associated with SDSS and UKIDSS sources, there are further columns listing optical and NIR properties, as detailed in F18.

SPIRE wavebands and 7% for PACS (see V16 for more details).

5. The Catalogs

We included all sources in the catalogs that were detected above 4σ in one or more of the three SPIRE bands: 250, 350, and 500 μm. We eliminated all sources from the original list of point sources produced by MADX if they fell within the aperture of an extended source. The parameters available for each source are listed in Table 3. If a source is included in the 4σ catalog, flux measurements are presented for all bands, with no censorship at low signal-to-noise. This means that some flux measurements are negative; these are not flagged in any way, but simply listed with the corresponding uncertainty.

Since the PACS instrument is not exactly aligned with the SPIRE instrument, there are some sources in the catalog that have no PACS coverage; the PACS fluxes for these sources are flagged as -1. (No real sources have measurement <-0.3 Jy, so there is no possibility of confusion between the flagged sources and negative flux measurements).

All of the H-ATLAS fields were observed at least twice, making it possible to search for moving sources such as asteroids. We found nine asteroids in the GAMA fields (V16), eliminating these from the final catalog. We carried out the same search for the NGP and SGP but found no moving objects. Both the NGP and SGP fields are at much higher ecliptic latitude than the GAMA fields, so it is perhaps not surprising that we find no more solar-system objects.

Table 4
Stars Detected in H-ATLAS

Name	Position
EY Hya	08:46:21.4 +01:37:53
IN Hya	09:20:36.7 +00:10:53
NU Com	13:10:08.5 +24:36:02
19 PsA	22:42:22.3 −29:21:43
V PsA	22:55:19.9 −29:36:48
S Scl	00:15:22.4 −32:02:44
XY Scl	00:06:35.9 −32:35:38
eta Scl	00:27:55.9 −33:00:27
Y Sci	23:09:05.7 −30:08:04
HD 119617	13:43:35.2 +35:20:45
R Sci	01:26:58.2 −32:32:37
Fomalhaut	22:57:39.2 −29:37:22

The sources in the final catalogs are almost all extragalactic sources. We carried out a search for clusters of sources in all the H-ATLAS fields (Eales et al. 2018, in preparation). In the GAMA9 field, we found several groups of sources that are likely to be clusters of pre-stellar cores, implying that the catalog for this field is likely to contain a few tens of Galactic sources. However, we found no similar clusters in the other fields, which makes sense, since the GAMA9 field is at a much lower Galactic latitude than the other fields. Pre-stellar cores are therefore likely to be a very minor contaminant to the catalogs for these fields. There are a few debris disks and AGB stars in the catalogs, and an incomplete list is given in Table 4. However, well over 99% of the sources are

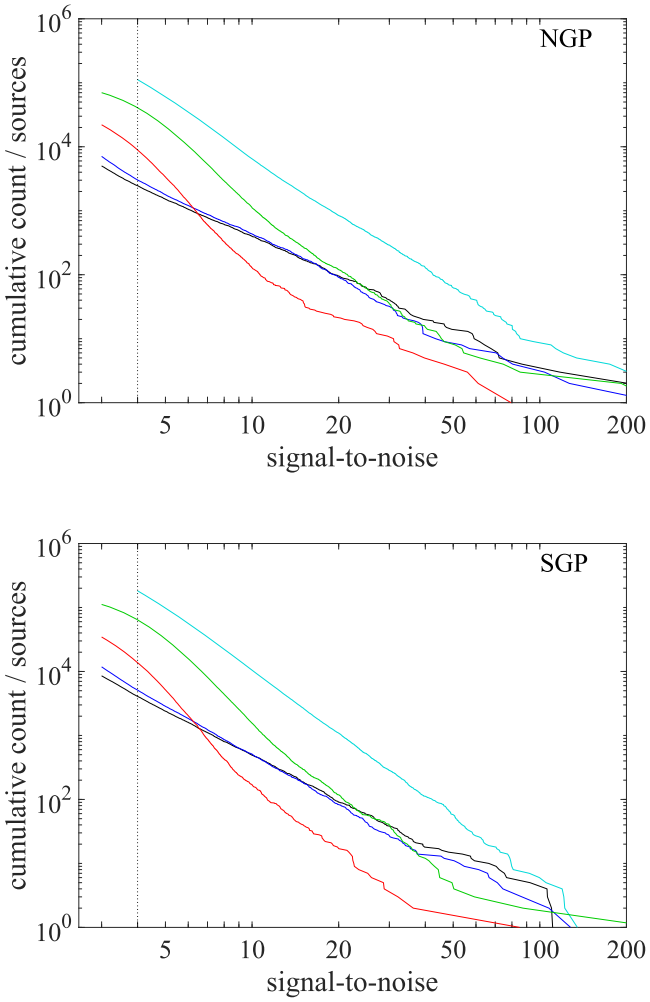

Figure 7. Cumulative number of sources as a function of signal-to-noise at 100 μm (black), 160 μm (blue), 250 μm (cyan), 350 μm (green), and 500 μm (red). The NGP area is shown in the top panel, and the SGP area is shown in the bottom panel. The vertical dotted line shows the 4σ limit for the 250 μm selection. The other bands are truncated at 3σ.

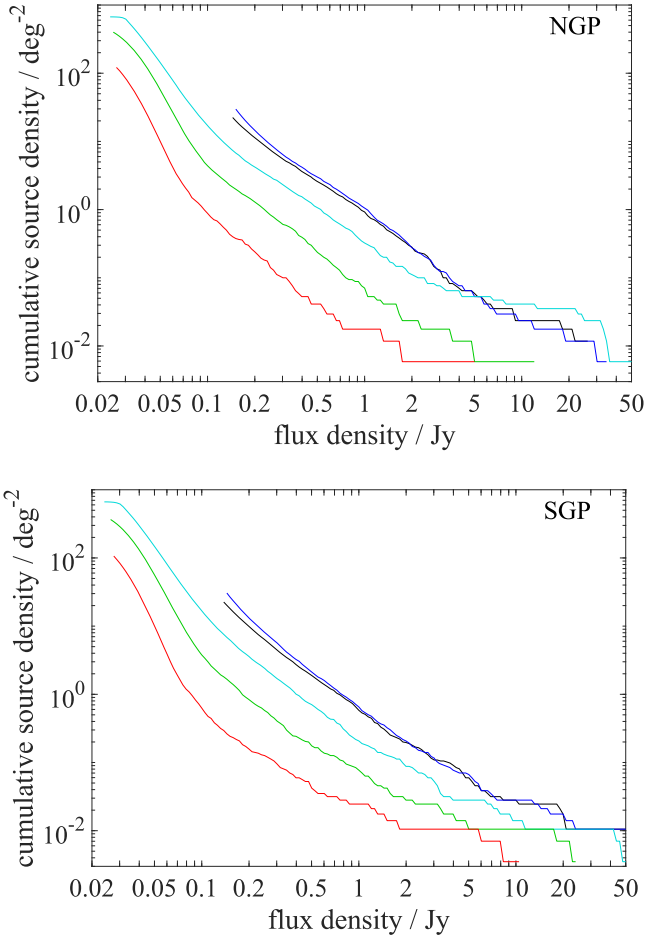

Figure 8. Cumulative number of sources as a function of flux density at 100 μm (black), 160 μm (blue), 250 μm(cyan), 350 μm (green), and 500 μm (red). The NGP area is shown in the top panel, and the SGP area is shown in the bottom panel. The counts are plotted only above the limit of 3σ in each waveband.

extragalactic. The extragalactic sources range from galaxies at redshift 6 (Fudamoto et al. 2017) to nearby galaxies, such as the spectacular spiral galaxy, NGC 7793, which is in the center of the SGP, and one of the brightest galaxies in the nearby Sculptor group.

5.1. Statistics of the Catalogs

The catalog for the NGP covers 177.1 deg^2 and contains 118,980 sources, of which 112,069 were detected at >4σ at 250 μm, 46,876 were detected at >4σ at 350 μm, and 10,368 were detected at >4σ at 500 μm. The effective sensitivity of the PACS images was much less, but the catalogs contain flux density measurements at 100 and 160 μm for all the sources in the catalog, even if the measurements were negative. 5036 sources were detected at >3σ at 100 μm and 7046 sources were detected at >3σ at 160 μm.

The catalog for the SGP covers 303.4 deg^2 and contains 193,527 sources, of which 182,282 were detected at >4σ at 250 μm, 74,069 were detected at >4σ at 350 μm, and 16,084 were detected at >4σ at 500 μm. 8598 sources were detected at >3σ at 100 μm and 11,894 sources were detected at >3σ at 160 μm.

The cumulative number of sources as a function of signal-to-noise in the five bands is shown in Figure 7. The 250 μm band is the most sensitive, and has the largest number of detected sources. Of the PACS bands, the 160 μm band detects more sources above 3σ.

The observed number of sources as a function of flux density in the PACS and SPIRE bands is shown in Figure 8. Note that this shows the observed flux in the catalog, before any corrections are made for the source SED (Section 4.3) or "flux boosting" (Section 5.3), which are necessary before the flux densities are compared with model predictions.

5.2. Positional Accuracy

V16 carried out extensive simulations to investigate the accuracy of the H-ATLAS catalogs by injecting artificial sources on to the GAMA images, and then using MADX to detect the sources and measure their flux densities and positions. The results of these "in-out" simulations apply to the NGP and SGP catalogs, which were produced using almost exactly the same methods.

We investigated the accuracy of the source positions in two ways: (1) by looking at the positional offsets between the *Herschel* sources and galaxies found on optical images; (2) from the in-out simulations. Bourne et al. (2016) and F18

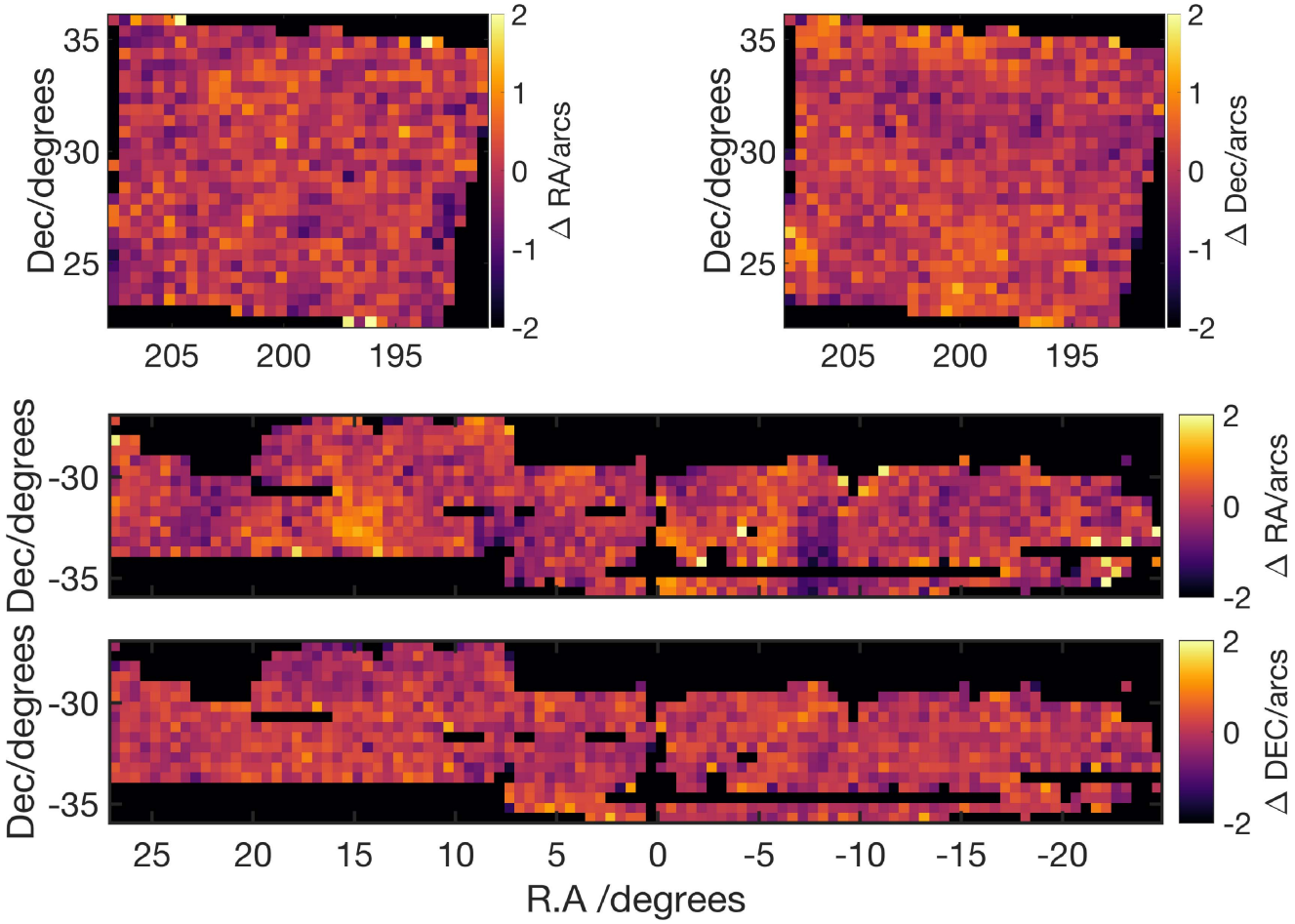

Figure 9. Mean positional errors in R.A and decl., averaged in areas 0.°5 ×0.°5 as a function of position on the sky for the NGP and SGP fields.

described the details of the first method, which takes into account the clustering of the galaxies in the optical catalog and the PSF of the *Herschel* observations. Note that astrometric offsets were first calculated using catalogs from individual *Herschel* observations. The astrometry for each observation was updated before creating the final maps (S17).

In the case of the NGP, we applied this method using the galaxies found in the SDSS *r*-band images (F18), which thus ultimately ties the *Herschel* positions to the SDSS astrometric frame. In the case of the SGP, we used the galaxies found in the VLT Survey Telescope ATLAS (Shanks et al. 2015), which thus ultimately ties the astrometry in the SGP to the astrometric frame of this survey. We find that the positional error, $\sigma_{\rm pos}$, varies from 1.2 to 2.4 arcsec, as the signal-to-noise in flux varies from 10 to 5, with a relationship between positional accuracy and flux density given by $\sigma_{\rm pos} = 2.4({\rm SNR}/5)^{-0.84}$. This agrees well with the errors in the measured positions of the artificial sources in the in-out simulations (V16). Note that the uncertainty on the optical positions is typically 0.1 arcsec, and thus is negligible compared to the *Herschel* uncertainties.

The mean positional errors as a function of position within the NGP and SGP fields are shown in Figure 9. Though there are hints of systematic variations in different parts of the fields, these are around 1 arcsec, which is less than the quoted absolute pointing accuracy of *Herschel* of ≃2 arcsec (Pilbratt et al. 2010).

5.3. Purity, Flux Boosting and Completeness

The catalog is a 4σ catalog, so we can use Gaussian statistics to predict the number of sources that will actually be noise fluctuations; on this basis we expect ≃0.13% of the sources in the catalog to be spurious. However, V16 argue that this is likely to be a slight overestimate because our errors, while being good estimates of the errors on the flux measurements, will underestimate the signal-to-noise of a detection. To explain in more detail, our estimate of the confusion noise for a source increases with increasing source flux, so the noise used to estimate the actual flux uncertainty is larger than the noise would be for a flux of zero, as would be appropriate to determine the significance of a detection. Thus, a flux that is four times our quoted error may correspond to, say, a 4.1σ detection. In this case our approximation of contamination from the 4σ tail of a Gaussian should be the 4.1σ tail. In practice, the contamination is so small that the difference is not important and we have not quantified it.

A major problem in submillimeter surveys, where source confusion is usually an issue, is flux bias or "flux boosting," in which the measured flux densities are systematically too high. V16 used the in-out simulations to quantify this effect in the H-ATLAS. Table 6 in V16 gives estimates of the flux bias as a function of flux density for all three SPIRE bands. The table shows that at the 4σ detection flux density, the measured flux densities are on average higher than the true flux densities by ≃20%, 5%, and 4% at 250 μm, 350 μm, and 500 μm,

respectively. Astronomers interested in comparing the flux densities in the catalog with the predictions of models should be aware of this effect. Following V16, we make no corrections for this in our catalog, but Table 6 in V16 can be used to correct the flux densities for this effect.

Note that the flux limit for a significant PACS detection is much brighter than the confusion limit, so PACS fluxes are not affected by confusion noise. Also, the 250 μm noise is so much lower than the PACS noise that the 250 μm selection should not introduce any significant incompleteness in the PACS sample. The PACS sample should have completeness and purity, as expected for the quoted Gaussian noise in the flux measurements.

V16 also used the in-out simulations to estimate the completeness of the survey as a function of measured flux density in all three SPIRE bands. This is shown in Figure 21 of V16 and listed in Table 7 of V16. The completeness at 250 μm is 87% at the 4σ detection limit of the survey.

6. Summary

We have described the construction of the source catalogs from the *Herschel* survey of fields around the north and south Galactic poles. This survey, which was carried out in five photometric bands—100, 160, 250, 350, and 500 μm—was part of the *Herschel* Astrophysical Terahertz Large Area Survey (H-ATLAS), a survey of 660 deg^2 of the extragalactic sky. Our source catalogs cover 303 deg^2 around the SGP and 177 deg^2 around the NGP.

The catalogs contain 118,980 sources for the NGP field and 193,527 sources for the SGP field detected at more than 4σ significance in any of the 250 μm, 350 μm, or 500 μm bands. We present photometry in all five bands for each source, including aperture photometry for sources known to be extended. We discuss all the practical issues—completeness, reliability, flux boosting, accuracy of positions, accuracy of flux measurements—necessary to use the catalogs for astronomical projects.

P.C., L.D., H.L.G., S.J.M. and J.S.M. acknowledge support from the European Research Council (ERC) in the form of Consolidator Grant COSMICDUST (ERC-2014-CoG-647939, PI H L Gomez). S.J.M., L.D., N.B., and R.J.I. acknowledge support from the ERC in the form of the Advanced Investigator Program, COSMICISM (ERC-2012-ADG 20120216, PI R.J. Ivison). E.V. and S.A.E. acknowledge funding from the UK Science and Technology Facilities Council consolidated grant ST/K000926/1. M.S. and S.A.E. have received funding from the European Union Seventh Framework Programme ([FP7/2007-2013] [FP7/2007-2011]) under grant agreement No. 607254. G.D.Z. acknowledges financial support from ASI/INAF and ASI/University of Roma Tor Vergata n.∼2014-024-R.1 and n. 2016-24-H.0

The *Herschel*-ATLAS is a project carried out using data from *Herschel*, which is an ESA space observatory with science instruments provided by European-led Principal Investigator consortia and with important participation from NASA.

ORCID iDs

S. J. Maddox https://orcid.org/0000-0001-5549-195X
P. Cigan https://orcid.org/0000-0002-8736-2463
M. W. L. Smith https://orcid.org/0000-0002-3532-6970
S. Dye https://orcid.org/0000-0002-1318-8343
C. Furlanetto https://orcid.org/0000-0001-6838-431X
G. de Zotti https://orcid.org/0000-0003-2868-2595
R. J. Ivison https://orcid.org/0000-0001-5118-1313
D. Scott https://orcid.org/0000-0002-6878-9840
I. Valtchanov https://orcid.org/0000-0001-9930-7886

References

Bourne, N., Dunne, L., Maddox, S. J., et al., et al. 2016, MNRAS, 462, 1714
Chapin, E. L., Chapman, S. C., Coppin, K. E., et al. 2011, MNRAS, 411, 505
Dunne, L., Gomez, H. L., da Cunha, E., et al. 2011, MNRAS, 417, 1510
Eales, S., Smith, D., Bourne, N., et al. 2018, MNRAS, 473, 3507
Eales, S. A., Smith, M. W. L., Wilson, C. D., et al. 2010, PASP, 122, 499
Franceschini, A., Toffolatti, L., Mazzei, P., et al. 1991, A&AS, 89, 285
Fudamoto, Y., Ivison, R. J., Oteo, I., et al. 2017, MNRAS, 472, 2028
Furlanetto, C., Dye, S., Bourne, N., et al. 2018, MNRAS, 476, 961 (F18; Paper III)
Griffin, M. J., Abergel, A., Abreu, A., et al. 2010, A&A, 518, L3
Griffin, M. J., North, C. E., Schulz, B., et al. 2013, MNRAS, 434, 992
Hunt, L. K., Draine, B. T., Bianchi, S., et al. 2015, A&A, 576, A33
Ibar, E., Ivison, R. J., Cava, A., et al. 2010, MNRAS, 409, 38
Neugebauer, G., Habing, H. J., van Duinen, R., et al. 1984, ApJ, 278, L1
Pascale, E., Auld, R., Dariush, A., et al. 2011, MNRAS, 415, 911
Pearson, E. A., Eales, S., Dunne, L., et al. 2013, MNRAS, 435, 2753
Pilbratt, G. L., Riedinger, J. R., Passvogel, T., et al. 2010, A&A, 518, L1
Planck Collaboration XXVI 2016, A&A, 594, 26
Poglitsch, A., Waelkens, C., Geis, N., et al. 2010, A&A, 518, L2
Rigby, E. E., Maddox, S. J., Dunne, L., et al. 2011, MNRAS, 415, 2336
Shanks, T., Metcalfe, N., Chehade, B., et al. 2015, MNRAS, 451, 4238
Skrutskie, M. F., Cutri, R. M., Stiening, R., et al. 2006, AJ, 131, 1163
Smith, D. J. B., Dunne, L., Maddox, S. J., et al. 2011, MNRAS, 416, 857
Smith, D. J. B., Dunne, L., Maddox, S. J., et al. 2017, ApJS, 233, 26 (S17; Paper I)
Smith, M. W. L., Gomez, H. L., Eales, S. A., et al. 2012, ApJ, 748, 123
Valiante, E., Smith, M. W. L., Eales, S., et al. 2016, MNRAS, 462, 3146 (V16)
Valtchanov, I. (ed.) 2017, The SPIRE Handbook, HERSCHEL-HSC-DOC-0798, v3.1
Zavala, J. A., Aretxaga, I., Dunlop, J. S., et al. 2018, NatAs, 2, 56